Development of a computer vision-based measuring system for investigating the porous media structure

T.A. Ruzova, B. Haddadi [*], T. Jonach, C. Jordan, M. Harasek

TU Wien, Institute of Chemical, Environmental and Bioscience Engineering, Vienna, Austria

A B S T R A C T

Porous materials are widely used in a variety of scientific and technological fields; therefore, a large number of publications deal with the challenges related to studying the porous media microstructure. Porosity investigation methods based on the measurement of certain physical properties of the medium are usually very complex, expensive, cumbersome, require harsh experimental conditions and are unable to determine pore size distribution. On the other hand, modern optical measuring techniques are also not universal and often need significant adaptation.

In this regard, a strategy is developed that formalizes the process of direct porosity measurement of the investigated specimen using a series of its images. The proposed method performs image denoising, aggregates separation, measurement of microstructure elements and mathematical analysis of acquired data. Numerical experiments performed using CT images of a porous ceramic sample suggest the reliability of the developed technique.

1. Introduction

In recent years, the industry of composite porous materials witnessed rapid growth. In particular, ceramic matrix composites are widely used in various technical processes. They find applications as a part of gas filters, thermal protection systems, refractory furnace linings, biomaterials etc. Key characteristic of composites is their porosity. Porosity affects various properties of the material, such as the mechanical and thermal properties, its structure, strength, mechanical behavior, impregnation rate, heat resistance, gas permeability, and other critical properties [1–4]. Therefore, porosity measurement is highly relevant for many areas of industry, science and technology.

For example, in metallurgical industry, special attention is paid to investigation of the pore structure characteristic of applied composites, since the pore size distribution pattern determines thermo-mechanical properties of the refractory castables and affects the stability of furnace insulation [5].

In construction, using resources efficiently and energy-saving problems is directly related to establishing concrete's pore patterns and developing mechanisms for target-directed impact on cement matrix formation [6,7]. Therefore, according to recent investigations, pores in the range of 20–50 nm have a greater effect on compressive strength than pores with a diameters more than 100 nm [8].

In pharmaceuticals, the porosity of the drug vehicle (medium in which active substance is formulated and/or administered) directly influences the release of the active ingredient, which is critical for extended-release products [3]. Since the drug release is based on molecular diffusion from the polymer matrix, the nature and velocity of this process are mainly governed by the polymer pore geometry. Therefore, the adjustment of the drug vehicle pore depth and diameter is the most common strategy to control drug release from mesoporous materials.

Porosity also determines the structure and strength of bone tissue, as well as the mechanical behavior of permeable implantable materials, which are widely used in traumatology, orthopedics, surgery, dentistry, urology, and other fields of medicine [9].

Thus, the pore size distribution pattern is one of the most significant factors that determine the mechanical properties of zirconia ceramics, one of the most promising engineering and restorative materials. ZrO_2-based composites are traditionally used in the metallurgical industry, highly appreciated in the manufacture of thermal barrier coatings for gas turbines and diesel engines and are suitable for use in medicine especially for various bone and joint replacement units [10].

Therefore, the estimation of the total pore volume and pore size distribution is one of the most important problems to be solved for the

---

practical application of porous media. A large and growing number of publications have investigated the issues of porosity measurement. Traditionally, the pore size distribution is measured by sorbometry and mercury intrusion porosimetry methods. Both of them give a reliable estimate of the specific surface area of a porous structure.

The sorption technique is based on the phenomenon of gas condensation on the open (accessible to gas molecules) surfaces of adsorbents [11,12]. During the experiment, an adsorption isotherm is acquired, then by means of applying certain mathematical models, pore distribution of the sample can be obtained. This technique is relatively easy to implement and can provide an adequate estimate of the solids porosity. The most significant challenge associated with this approach is that sorption processes are rather time-consuming. According to some estimates, analysis can take up to 60 h [13]. It also should be noted that pore morphology has a significant impact on the measurement results. For example, on the walls of disordered open and wedge-shaped pores, adsorption/desorption processes are much faster than in narrow slit-like pores of the same volume (due to the inaccessibility of such pores) [14]. There are various equations expressing the relationship between the adsorption capacity of the material and its porous structure. These equations, based on different adsorption theories, may provide different results.

Mercury intrusion porosimetry technique is based on the measurement of the mercury volume penetrating a porous solid as a function of the applied pressure [15], which makes it possible to obtain information on the pore size distribution. The main advantage of this approach is that it is much faster compared to alternative pore size characterization methods. The measurement can be performed in two modes: scanning (pressure increases continuously) and time- or rate-equilibrated (pressure is held at each set point for a specified time period or until the rate of intrusion decreases below some prespecified value) [16] and the results obtained in both modes cannot be compared.

An obvious and significant drawback of the method are the high toxicity of mercury, impossibility of exhaust extraction of mercury from the sample. These disadvantages require the implementation of strict safety measures and development of special protocols for waste disposal. Other disadvantages include lack of a reliable estimation of the volume of air trapped in the pores, the impossibility of assessing dead-end paths and a high risk of deformation by membranes (ceramic, polymeric, etc.) investigation.

It should also be noted that both considered techniques have certain measurement range limitations. Thus, mercury porosimetry is applied in the pore diameter range 3–360 μm, while the sorbometry (physical adsorption of N_2 gas) technique - in the range of 0.35–300 nm [17].

Recently, the nuclear magnetic resonance (NMR) cryoporometry technique has been widely used to study the structure of porous media. The method of NMR cryoporometry is based on the fact that the melting and freezing temperatures of the liquids entrapped within pores are strongly dependent on pore sizes. The method allows to perform moderately fast measurements (experiment usually takes about 3 h), characterized by high repeatability and good correlation with the results of adsorption methods. However, near the boundaries of the mesoporous range (2–50 nm), measurement accuracy decreases [18]. Among other limitations of the cryoporometry method, it should be noted that it has a narrow measurement range (2 nm–1 μm), need for special equipment for samples heating and cooling, and is characterized by a time-taking measurement process [19].

Therefore, the most significant limitations of so-called "physical" measuring methods are that they are rather laborious, time-taking, require harsh experimental conditions, are cumbersome and need expensive measuring devices. Besides, there may be significant variation between the data obtained using different techniques. The picture is further complicated by the presence of some additional factors affecting the measurement outcome, which makes it difficult to perform adequate structural analysis of porous material.

Recently, various optical techniques have become more widespread, because they can completely formalize the measurement process. Formalization is realized by transferring the measuring process to a computer screen, by using signal processing techniques and advanced mathematical tools. A number of publications [20 – 23] describe computerized video measuring systems suitable for various application fields in education, science and technology. The powerful functionality of modern intelligent measuring systems provides a wide spectrum of options for microstructural investigations. However, such systems are rather expensive, and their capabilities are limited by specific applications. Therefore, in some cases, these systems need to be adopted to enhance their measurement efficiency.

In the work of Quentin Libois etc. [21], optical porosity is introduced as a function of effective refractive index. However, one of the biggest challenges of this approach is that from the optical point of view, the difference between porosity and scattering phase function of the investigated material seems rather insignificant. This fact dramatically complicates the optical characterization of weakly absorbing materials and requires the development of new innovative approaches. To simulate the processes of light scattering in porous media, various mathematical models have been developed. Malinka [22] described a model that establishes relations between the scattering properties of the two-phase stochastic mixture, its microphysical characteristics and optical constants, considering the facets orientation and the ray path length inside solids or voids as independent variables. However, the authors note, that applicability of the model to any particular medium should be considered separately, based on the compliance with the experimental data.

Computed tomography (CT) is also widely used for porosity estimation and there is a vast array of publications dedicated to the subject. Therefore, the selection was narrowed down to focus on the most relevant literature. CT scanning is a non-invasive technology that allows to study internal structure of the specimens without destroying them. This feature makes CT one of the most popular investigation methods [24]. Combination of computed tomography with modern software allows to obtain high-precision and time-efficient results without the use of additional equipment. However, the quantitative assessment of the objects size, in particular pores, is complicated because of well-known Wicksell problem, which is the subject of a number of publications [25,26]. For the estimation of morphometric parameters of 3D objects, also the method proposed by Hildebrand and Rugsegger based on thickness mapping can be used [27].

Variability of optical properties and illumination parameters in different research areas does not allow to develop an image processing procedure of universal applicability and, as a rule, requires manual tuning of digital filters for each specific domain [28 – 29]. To date, there is no consensus in the scientific community about which segmentation technique is the most optimal for micro-objects (in particular, porous structures) images. On the contrary, a wide variety of publications devoted to the development of specialized algorithms in various fields indicates that the efficiency of image processing algorithms depends on the content area and research objectives [30].

Difficulties associated with the presence of defects, and the very nature of the raster presentation of graphical data requires the development of new approaches to estimate the many, at first glance, "trivial" parameters. A lot of unmet needs require further research in this area. In this regard, the goal of the proposed investigation is to develop a strategy that formalizes the processes of digital image processing, investigation of the porous media (in particular, samples of porous ceramics) structure, to acquire pore size distribution and statistical analysis of obtained data. The proposed approach may be used to guide designing hardware-software measuring systems for wide range of scientific and practical applications.

2. Materials and methods

The authors proposed a method for estimating the porosity of a sample using its CT scans. The main stages of the developed image processing strategy are described below.

2.1 Pre-processing. In this section the image preparations prior to the analysis are included (unpacking, brightness analysis etc). Images of complex structures (composite materials, emulsions, dispersions, etc.) are often darkened and low-contrast (Fig. 1a). The most common problem is an inefficient use of available quantization levels: the images are characterized by a narrow brightness range (Fig. 1b), which significantly complicates the process of microstructure investigation. Therefore, the original images usually need some pre-processing. To demonstrate the advantages of the proposed technique, CT-images (Fig. 1) of a porous ceramic sample (with a declared porosity of 40–50% and $d_{50} = 30$ μm) were used. This type of porous ceramics traditionally used for optimization of gas flows, accumulation/ retention of gas mixtures and for wide variety of other industrial applications. It has a complex microstructure that is typical for commonly used modern materials. So, using it as a test sample allow us fully reveal weak and strong points of proposed technique.

(a- CT image of the porous ceramics sample; b– brightness histogram)

Figure 2 shows a fragment of the image at high magnification, which illustrates the problems associated with low contrast and the lack of a well-defined pore boundary. However, the biggest challenge is the presence of a significant number of aggregated objects (pores). The presence of aggregates (of the particles, pores and drops) is a very common problem when imaging dispersions, emulsions and porous media [31,32]. Being interpreted as a single object, such an aggregate causes significant errors in analysis.

Rasterization of graphic information, i.e. its converting and storing in a computer as a set of equal small squares (so called "raster") can also cause significant errors in describing complex curves (curved pore boundaries). Fig. 2b demonstrates the raster organization of the investigated images (2a).

(a – C T-slice of the porous ceramic; b– Fragment of CT-slice at high magnification)

2.1. Field of view (FOV) selection and clipping

Whenever a series of sequential images is processed, the problem of spatial drift of the entire image or region of interest may arise, that requires certain corrective measures [33,34]. Often offset is caused by the slight deviation of the studied sample from the scanning *Z*-axis (Fig. 3a), i.e. by non-zero tilt angle. Preliminary analysis of the test images also revealed some drift of the working area to the right. Evaluation showed that the total displacement of the working area (the difference of the FOV position between the first and last images) for the test sample is

58.8 μm (Fig. 3b).

Due to the unstable position of the FOV, any pre-specified co-ordinates for its identification could not be used. Therefore, a method for automatic FOV detection should be developed.

The proposed technique consists of applying and gradually shifting the circle-shaped template of the FOV size in order to find a position, where the contribution of the background (percent of the black points inside the template area) is minimal. In other words, a position should be found where the function S_{black}/S_{sect} (S_{black}- total area of the black points, S_{sect} – section area) has a local minimum. A scheme of the process is presented in the Fig. 4. In this scheme the function S_{black}/S_{sect} (Fig. 4b) has local minimum when the template is applied in position 3, which matches the FOV location (Fig. 4a).

Figure 5 illustrates the application of this algorithm to a real photo (as the template shifts, gradual decrease in the area of black halo on the left side of the FOV is observed). The next step is clipping the field of view (or cropping the background) to reduce the amount of information to be processed. For the purpose of simplicity, we proceeded from the assumption that the FOV's shape and size in z-direction are fixed (for example, for cylindrical specimen). Otherwise, the algorithm requires some adoption, considering the nature of shape/size variations. In the practical implementation of the methodology, this issue was omitted to speed up the calculations.

2.2. Image segmentation

After selecting the work area, its segmentation is carried out. Image segmentation is the process of separating the objects of interest from the background considering their brightness level. Since the software is intended for dealing with a large number of images in a batch processing mode, the fastest algorithm should be chosen. Therefore, the authors used the image threshold-based segmentation technique [35], providing the fastest result. Thresholding technique in its simplest form consists of comparing the brightness value of each pixel $g(x, y)$ of the image with some pre-specified threshold *T*. As a result, original grayscale image with N brightness levels is converted into binary (black and white) form, having only two intensity values – 0 and 1.

$$\widetilde{g}(x,y) = \left\{ \begin{array}{l} 0, g(x,y) < T, \\ 1, g(x,y) \geq T \end{array} \right. \tag{1}$$

g (x,y) – brightness value at (x,y) point in original grayscale image;
$\widetilde{g}(x,y)$ – corresponding brightness value in resulting image;
T – fixed threshold value.

Although this approach is not always optimal, in this case this application is justified by the uniform lighting, absence of shadows and the low noise level that is generally typical for CT-scans. Therefore, fixed-level thresholding has been used. The brightness threshold value can be determined in various ways, for example on the base of an image histogram [35,36].In the case of unsatisfactory image quality or a small
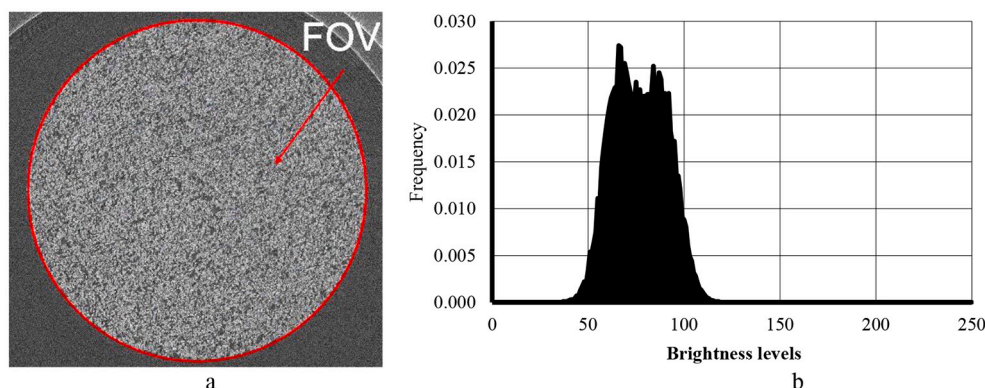

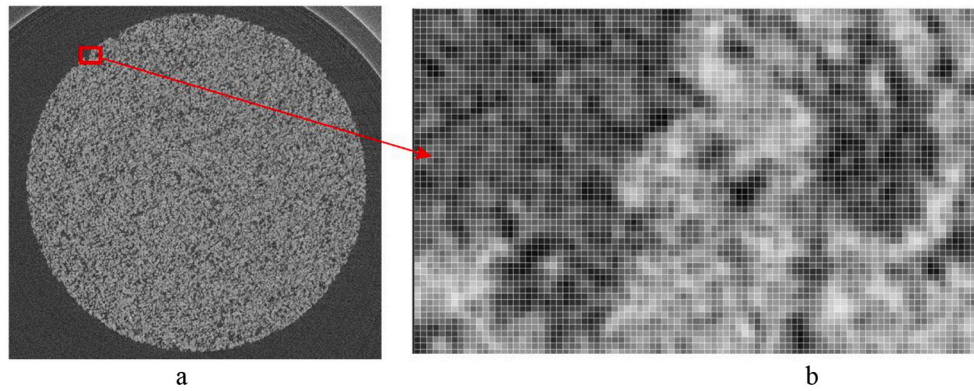**Fig. 1.** CT image of a porous ceramics sample (Field of View - FOV) and its brightness histogram.

Fig. 2. Fragment of the image at high magnification.
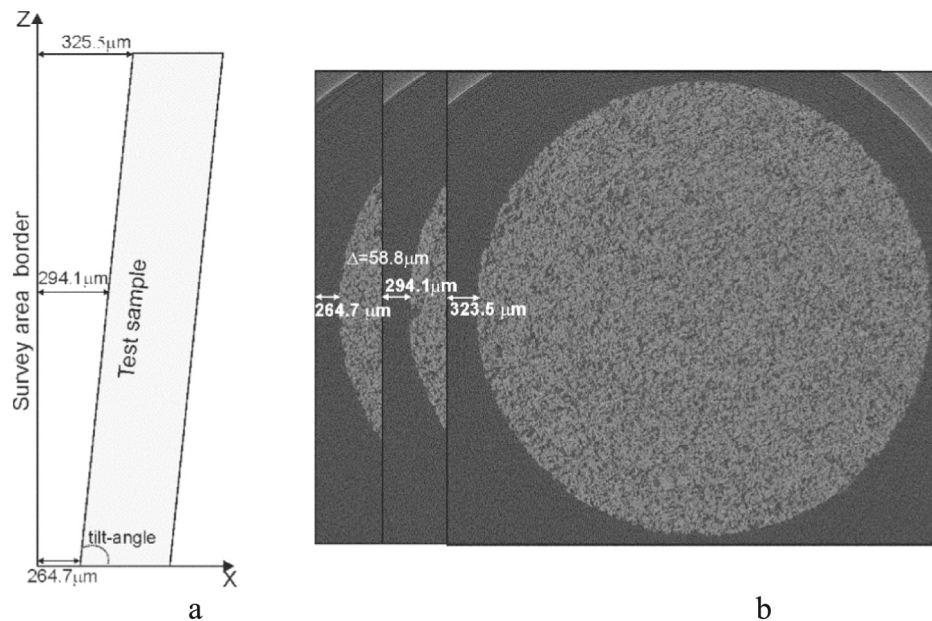

Fig. 3. FOV drift (a – nature of the FOV drift; b – displacement of the FOV in the test images).

series size (i.e., if runtime is not so critical), more complex adaptive segmentation algorithms, such as the two-pass thresholding method with a sliding window can be considered [36]]. These algorithms divide the image into several sections and specify for each section its own system of thresholds as a function of the brightness parameters for this particular area. Bandpass filters can also be used to remove noise.

2.3. Artifacts removal

Artifacts commonly occur in clinical and non-clinical CT images and can seriously complicate image interpretation, causing significant distortion of the visual information [37]. Therefore, special attention is paid to the development of effective methods for artifacts reduction. The authors propose an easy to implement technique for correcting one of the most common defects – ring or band artifacts, that appear as bright or dark circular bands. Such artifacts, as a rule, are caused by the increase in beam average energy level due to absorption and attenuation of X-rays when passing through dense structures (beam hardening effect). Sometimes dark bands may be caused by detector defects or miscalibration [36,38], in this case, the artifacts position is fixed and prespecified coordinates were used.

The most obvious solution is to apply a mask to the corresponding image area. However, this approach causes a violation of the structural

connectivity of the adjacent objects and, as a result, leads to an inadequate description of the sample structure. This fact is clearly demonstrated by the test images of the porous ceramic, which are obscured by this type of artifacts - dark concentric semicircles (Fig. 6) that can significantly affect measurement results (Fig. 7).

Therefore, it is suggested to remove artifacts by their partial destruction in order not to break the connectivity of the structures on both sides. Destruction of artifacts presented in Fig. 8a is carried out by randomly filling a certain fraction (20%) of points along the artifact line with white. As shown in Fig. 8b, the radial line is not completely erased and pores topology is preserved (Fig. 8c).

With this approach, artifacts removal is performed in two stages: first, they are fragmented into pieces, then the remnants that have lost their structural integrity are "washed out" using the morphological technique (image erosion and dilation) [39].

2.4. Preliminary pores separation and denoising

Dilation (morphological expansion) is the convolution of an image or its part with a certain structuring element (anchor) of arbitrary shape and size. The structuring element is applied to all pixels of the binary image. Each time when the original (usually central) pixel of the structural element is superimposed with a current pixel of the original
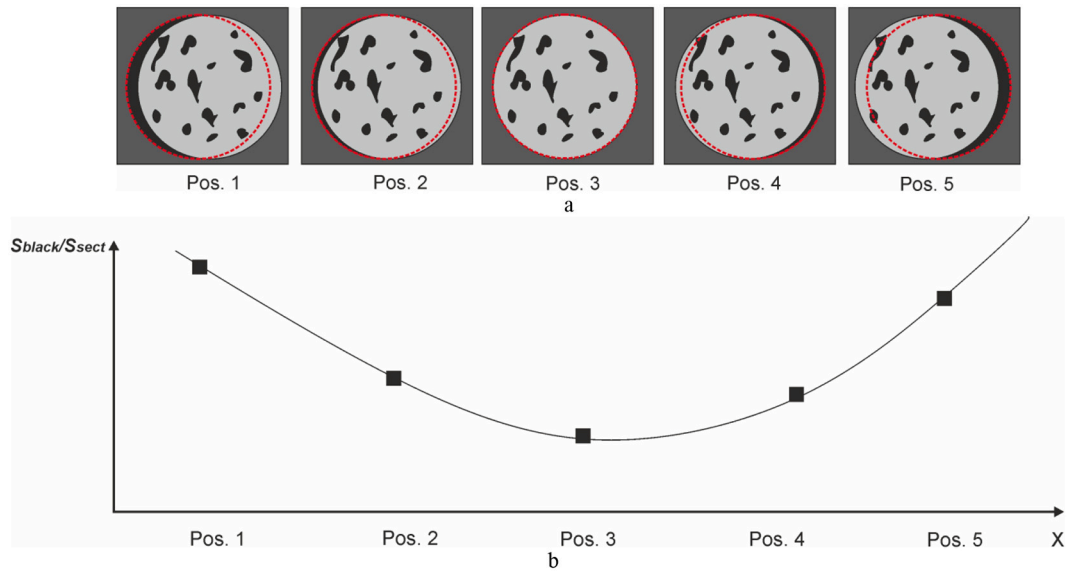
Fig. 4. Scheme of algorithm for automatic FOV searching.
(a–process of applying and gradually shifting the circle-shaped FOV template; b– contribution of the background at different template positions)
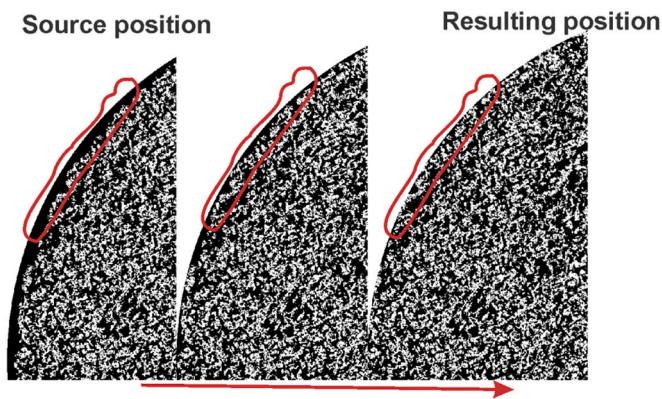

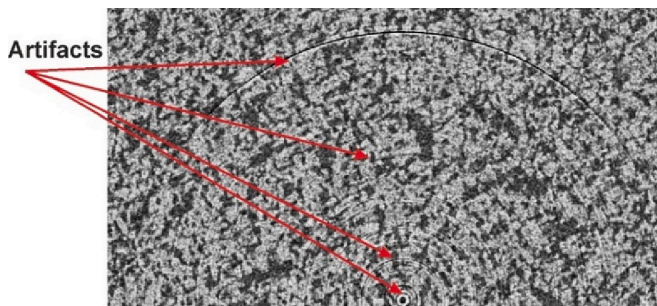**Fig. 5.** Application of algorithm for automatic FOV searching.

Fig. 6. Artifacts in the image of the porous ceramics sample.

Fig. 7. Attempt to remove artifacts by masking.
(a– masking artifacts in the source image; b– connectivity violation in resulting image;
for clarity, each object is assigned its own unique color, the principle is discussed below);

image, a logical disjunction of all pixels of the structuring element with the corresponding pixels of the binary image is performed. The results are placed in the output image, which is initialized to zero values.

Erosion (morphological shrinking) is a dual reverse operation. It allows to remove small elements of noise (including the remains of artifacts) and to separate pores aggregates in their "necks" (thin places). A side effect of this operation is that the remaining objects are reduced in size. To avoid this effect, an erosion operation with the same structuring element should be followed by dilation, which restores objects to their
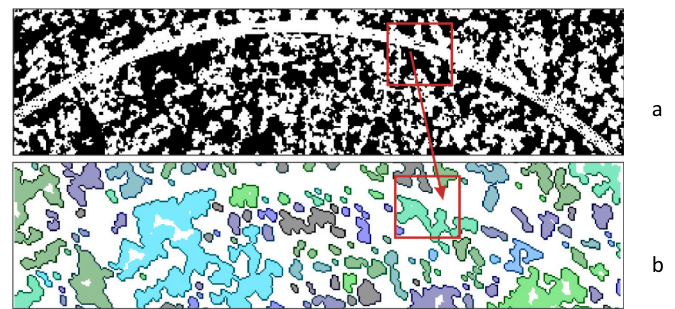
original size.

At this stage, two successive erosion operations are performed with structuring elements in the form of a square (■, Fig. 9b) and an oblique line (\, Fig. 9c), as well as two successive dilations with the same structuring elements (Fig. 9d and e). To avoid objects deformation as much as possible, structuring element of the minimum size (3×3) is applied. As the first "symmetrical" element (■) is used, it causes destruction of "extra" connections between the objects without any assumptions regarding their orientation. As it is shown in Fig. 9c, in the most cases, the noise on the objects edges has a pattern of oblique line, so it is reasonable to use structuring element of corresponding shape (\) at the next step. In our case, this combination of structuring elements, in comparison with other considered combinations, separated the aggregates most effectively. However, in each particular case, the choice of a structuring element should be based on the specifics of the particular image group.

a- initial image; b- 1st erosion operation; c- 2nd erosion operation; d- 1st dilation operation; e- 2nd dilation operation(resulting image).

In Fig. 10 an illustration of the base step of the process is given. Thus, at this stage, filtration and primary separation of aggregates are performed. As shown in Fig. 9 a and c, the resulting image is characterized by less noise. Areas circled in red in magnified fragments (Fig. 10b and d) show successful aggregates separation.
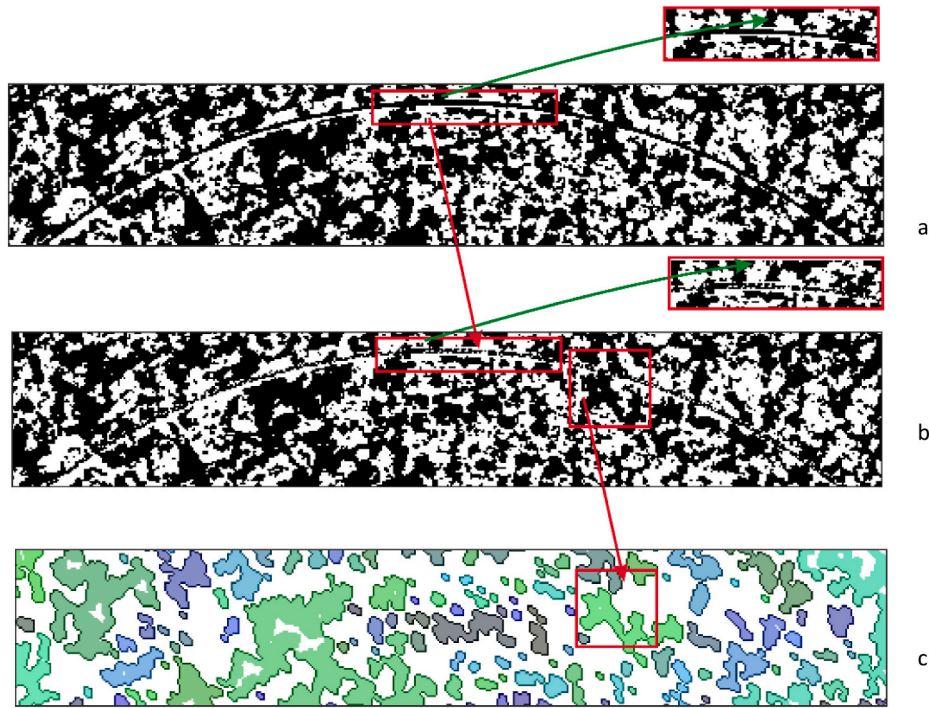
Fig. 8. Removing artifacts by partial destruction of the radial lines.
(a– source image, containing aggregates; b – image after partial aggregates removing; c – resulting image with identified pores –pores topology is preserved to maximum extent)
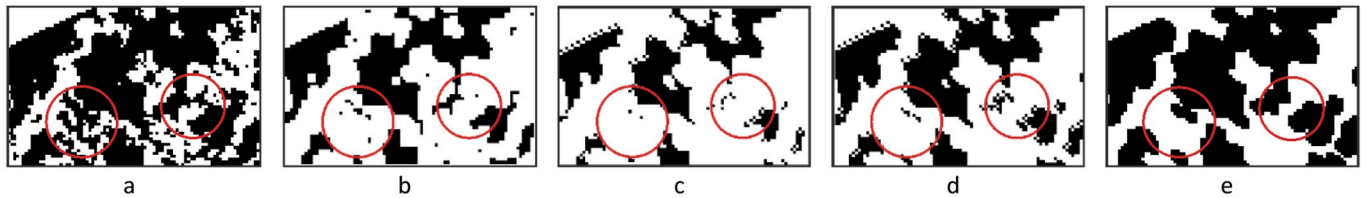

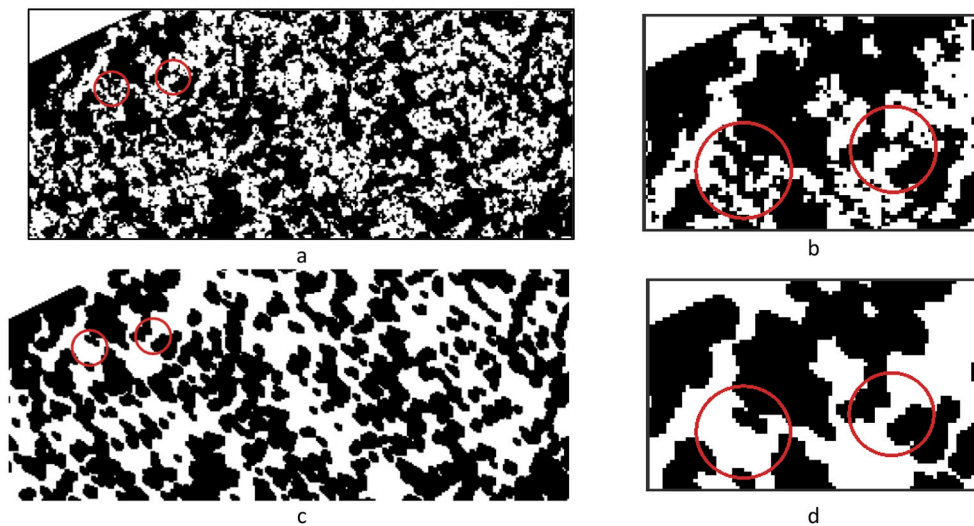**Fig. 9.** Step-by-step illustration of pores separation and denoising processes

Fig. 10. Preliminary pores separation and denoising (a –initial image; b – magnified fragment of initial image; c–resulting image; d – magnified fragment of resulting image), red circle marks corresponding areas in the source and resulting images to demonstrate method efficiency. (For interpretation of the references to color in this figure legend, the reader is referred to the web version of this article.)

2.5. Pores identification

Porous microstructures are characterized by the presence of a large number of complexly configured objects. To avoid confusion when processing such images, certain informative features should be specified as an unambiguous criterion to determine whether a certain pixel belongs to an object of recognition. This approach allows preserving the topology of the processed object. As such features, the color of the object's "body" and the color of its contour are chosen. Thus, when making a list of contour points coordinates, pixels that have different informative features (colors) will not be assigned to the same object. These colors should be unique for each object; corresponding color sets should be disjoint. Therefore, in terms of color system models, the subspaces defined by these colors should be non-overlapping. For routine processing of a large number of objects in the microstructure images, a simple mathematical description of these color spaces was proposed. A model was developed for selecting two non-overlapping subspaces of RGB color space. In the proposed model, R, G, B components of assigned colors in RGB space are expressed as functions of the object's serial number and can be easily calculated using simple formulas that does not significantly affect processing time:

$$B = N \bmod Base; \quad a_g = N \operatorname{div} Base;$$

$$G = a_g \bmod Base; \quad a_r = a_g \operatorname{div} Base;$$

$$R = a_r \bmod Base,$$

where

N – object's serial number;

$x \bmod y, \ x \operatorname{div} y$ – functions, that return the remainder and the quotient from integer division of the first argument x by the second argument y, respectively;

Base – arbitrary constant (in considered case is assigned to 128, see below),

In the RGB model, each primary color ranges from 0 to 255, therefore to select two non-overlapping subspaces in RGB space, it is proposed to vary components of the object's "body" color from 0 to 127 (i.e., constant *Base* should be assigned to 128). For synthesizing the contour color to the components of the corresponding "body", color value 128 should be added. Such selection is very suitable for processing fractal structures and visual analysis of their outer contour. A detailed description of the model is given in [40,41]. A schematic representation is given in Fig. 11c. Such a system allows to detect more than 2 million objects in single image. Two-color identification is suitable for processing structures of complex morphology, including fractals, and for visual analysis of their outer contour. The result of the model application is shown in Fig. 11a and b. In Fig. 11d, a fragment of a processed image is presented. As can be seen, a unique color is assigned to each object, which allows to visually assess the pore's topology and eliminate their confusion when establishing belonging of a considered pixel to a particular object.

When a connected set of points corresponding to a certain micro-object or micro-objects aggregate is detected and marked with a unique color, an ordered list of contour points of the identified figure is formed. For this, a method for automatic contour tracing has been developed. The method consists of choosing the reference point of the contour and identifying the nearest point having the same color that is assigned to the "body" or contour of the considered object. The method is based on the idea described in [42] for processing multi-connected regions and constructing simply connected contours. To make the choice of the next contour point unambiguous, a set of rotation vectors is introduced (Fig. 12a). The order of these vectors specifies the sequence of neighboring points to be processed (same order of vectors should be applied to each object).

Therefore, the selection of every next contour point is carried out by sequential enumeration of the adjacent pixels with the given brightness parameters according to the rotation vector's order. The next point of the contour is a pixel specified by a vector with the minimal number (8-connectivity pattern is used). The contour tracing algorithm stops, if it returns to the starting point. In combination with the above mentioned 2-color identification system (where color is a criterion determining whether a certain pixel belongs to identified object or not), this approach eliminates ambiguous vector selection. A detailed description of this procedure is given in [43,44]. Fig. 12b illustrates application of this technique.

2.6. Local (final) separation of large objects

Unfortunately, the object-separation procedure, does not always provide a satisfactory result as in Fig. 13a. For example, the object marked in red in Fig. 13b still has a large number of connections, that may be a sign of insufficient efficiency of the separation procedure that obscures the measurement results (internal holes like the "hole" in the gray-colored object were not considered).

However, further non-selective application of morphological operations to the entire image is inappropriate, since it can cause distortion of the objects' contours. Therefore, at the next stage the authors perform selective separation of aggregates which size (in terms of area-equivalent diameter) exceeds a certain pre-specified threshold value.
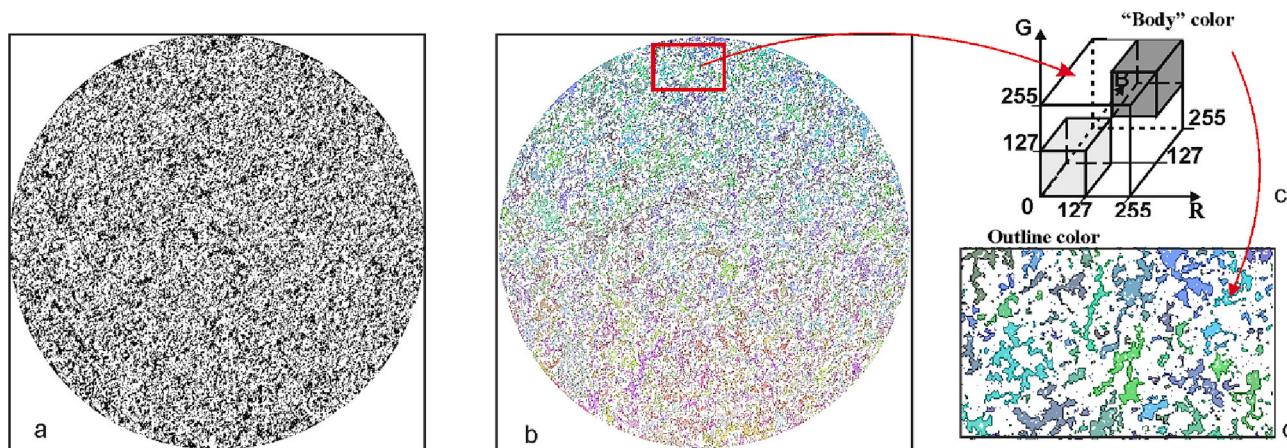

Fig. 11. Efficient pores selection by means of two-color identification technique.
(a – initial image; b – resulting image; c– model for selecting two non-overlapping subspaces of RGB color space;
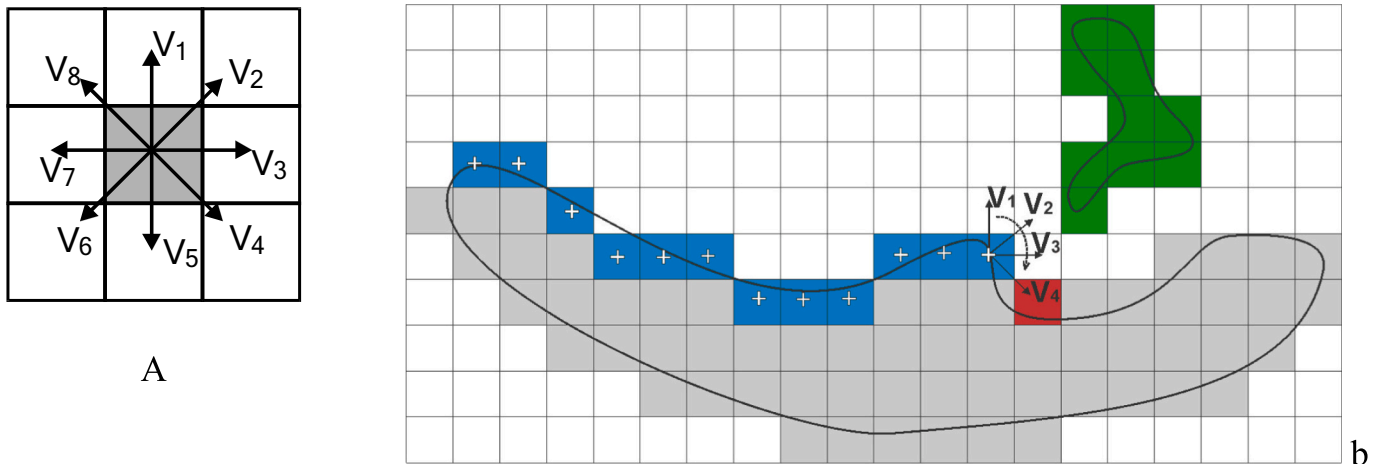d – magnified fragment of the resulting image.

Fig. 12. Construction of simply-connected contour using elementary rotation vectors a) Set of elementary rotation vectors; b) Contour tracing procedure (pixels corresponding to the considered object are marked in gray; pixels forming another object are marked in green; plus (+) signs on blue background represent pixels that have been already included in the list of contour points; point in question is marked in red). (For interpretation of the references to color in this figure legend, the reader is referred to the web version of this article.)
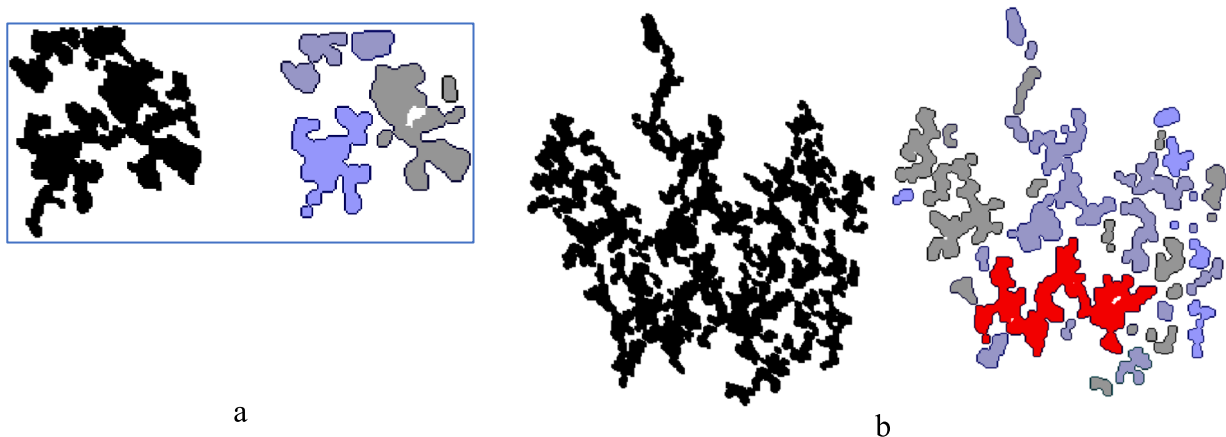

Fig. 13. Examples of successful (a) and unsuccessful separation (b) (red color indicates the object that may need further separation). (For interpretation of the references to color in this figure legend, the reader is referred to the web version of this article.)

To increase the efficiency of this process, morphological separation of the selected objects is performed by other structuring elements – in the form of a square (■) and a plus (+). The principles of structuring elements selection are similar to those described in paragraph 2.5. Therefore, in this stage target separation is performed.

However, some aggregates cannot be separated even in this case, since they have sufficiently stable (wide) connections. Therefore, it makes sense to experiment by preprocessing some part of the images with different thresholds (i.e. different values of minimum size of aggregates to be separated) and then choose an optimal threshold value by comparing the measurement results with the pre-specified (control) parameters. For example, for the test samples, three variants of separation were applied with pore separation thresholds of 200 μm, 150 and 120 μm.

2.7. Obtaining the resulting image

In Fig. 14, the resulting images are presented. The resulting image is a superimposition of identified pore contours on the source image. The figure shows two variants of processing the same original source (Fig. 14a). In the left figure (Fig. 14b), pores over 200 μm are separated, and in the right figure (Fig. 14c) – pores over 150 μm are separated. The bottom photo (Fig. 14d) shows that after artifacts removal pores

topology is preserved.

2.8. Measuring and statistical analysis

Since the computer is an inseparable part of most modern measuring systems, it makes sense to consider the error introduced by the computer as a measuring tool. As for bias connected with threshold selection, if fixed-level technique is used, the same threshold value is applied to all images and the associated error can be considered systematic. When adaptive algorithms are applied, threshold value is determined automatically and operator's influence is completely excluded. Unfortunately, it is beyond author's power to eliminate all systematic errors. In the current study, we deal with the bias associated with analog video sampling.

Using a computer as a measuring tool introduced an error. The reason for it is that the analogue video signal is split by the computer and converted into a raster of equal small squares, which causes a systematic bias in the assessment of areas and perimeters. The nature of this bias is illustrated in Fig. 15.

To consider this error, authors propose an approximation model for describing perimeter of a planar figure that significantly reduces measurement error [43,44]. According to this model the perimeter is represented as
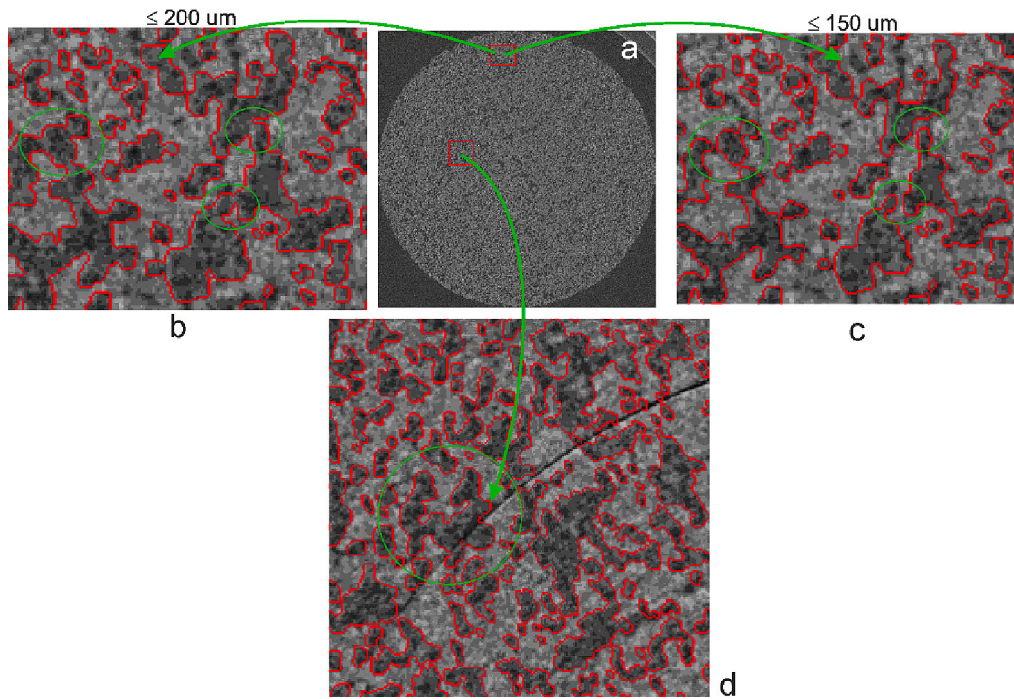
Fig. 14. Resulting image. a) source image; b) Pores over 200 μm are separated; c) Pores over 150 μm are separated (areas where the difference between these two options is the most noticeable are marked in green); d) artifact area (the area marked in green demonstrates that the object topology in artifact overlapping region is preserved).
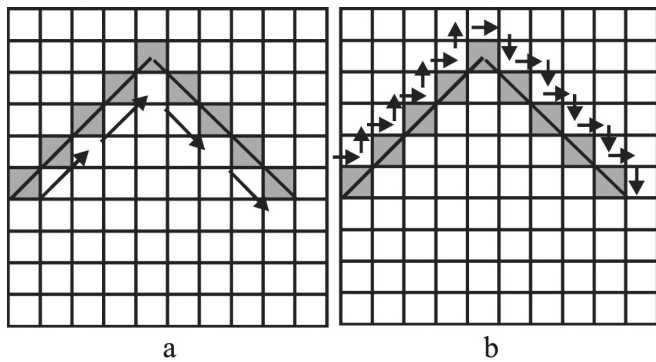

Fig. 15. Measurement error associated with raster nature of visual data (a–true perimeter; b –staircase effect).

$$P = \sum_{i=1}^{n} \beta_i \Delta P_i \qquad (2)$$

where $\Delta P_i = \sqrt{(\Delta x_i)^2 + (\Delta y_i)^2}$ – perimeter of elementary contour segment;

$\Delta x_i = x_i - x_{i-1}$ – the distance between the centers of ajascent pixels;

y_i – y-coordinate of the current pixel;

N – number of the border points.

β_i– smoothing coefficient, that was determined experimentally.

Figure 16 presents β as a function of contour inclination angle for different image resolutions. For a square oriented at an angle of 45° to the raster lines, this model reduces the maximum measurement error from 41% to 1% [43,44].

As shown in [43], the maximum error for the border section of any figure oriented at an angle of $\pi/4$ to the raster lines is $(2 - \sqrt{2})/\sqrt{2} =$
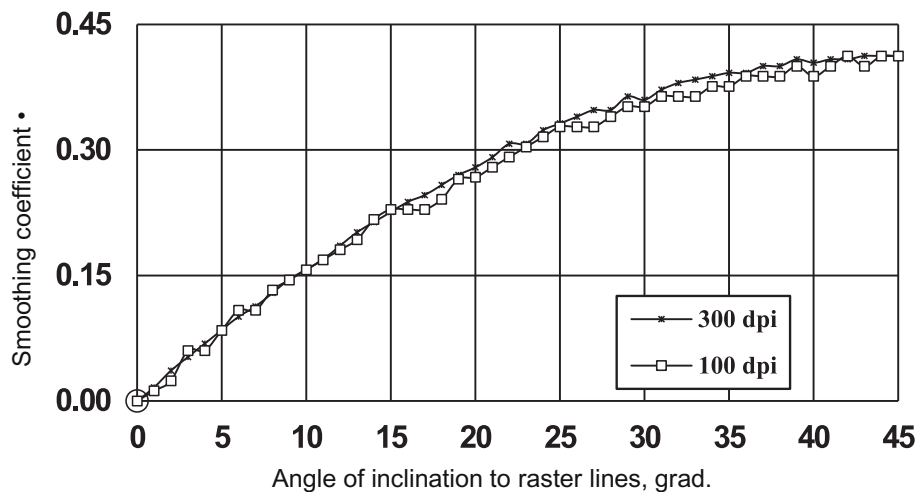

Fig. 16. Coefficient β as a function of contour inclination angle.

0.414, regardless of the figure's size. In real cases, the error varies from 0 to 0.414, depending on the angle of the contour inclination to the raster grid. The local contour inclination angle is evaluated by the slope of the line, approximating the corresponding contour section.

Then porosity is estimated: at first, it was evaluated the total pore area, taking into account the error introduced by the staircase effect, and then porosity was calculated as the ratio of the total pore area to the area of the cross-section.

To obtain the statistical characteristics of the pore matrix, mathematical processing of the acquired pore sizes was carried out. The entire series of CT slices (300 Gy-scale images, 1867×1773 pixels, resolution 340.4 pixels/mm) was processed, pores contours were detected, and pore diameters were calculated. Acquired data were merged into a single data set.

To obtain brief descriptive coefficients that summarize data set, a primary statistical analysis of the sample was performed. The sample was divided into classes. The number of classes was calculated according to Sturges rule [45]:

$$k = 1 + 3.322 \log n,$$

where.

    k = the number of classes;

    n – the number of observations in the data set.

For each class the frequencies, midpoints, relative frequencies, cumulative relative frequencies (empirical distribution function values), as well as the empirical probability density values were evaluated.

Adjacent intervals with frequency less than 5 were merged [45,46]. For clarity, the results are presented in the form of graphs of the empirical distribution function and the empirical probability density functions.

2.9. Technique for outlier detection and removal

To confirm the robustness of obtained distribution parameters, large (potentially agglomerated) objects are treated as sample outliers. It should be noted that this approach is applied strictly formally (without considering the nature of such aggregation and applicability of the procedure from the physical point of view). There are multiple ways to detect and remove the outliers, but the main problem is their dependence on the distribution pattern of the investigated data. As a rule, the authors start from the assumption of normality. In this case, a method is needed that is least dependent on the distribution type.

One of such methods [45] involves evaluation of not only the traditional distribution center $\overline{x}$, but also four other estimates:

median $x_m = x_{0.5}$–50th percentile of the empirical distribution;

$$x_c = (x_{0.25} + x_{0.75})/2 \ ; \ - \text{ the folds center;}$$

$$x_p = (x_{min} + x_{max})/2 \quad \text{–range center and}$$

$$\overline{x_{0.5}} = \frac{2}{n} \sum\nolimits_{[n/4]}^{[3n/4]} x_i$$

–arithmetic mean of 50%of the central observations,where $x_{0.25}$ and $x_{0.75}$ – 25% and 75% percentiles, respectively;
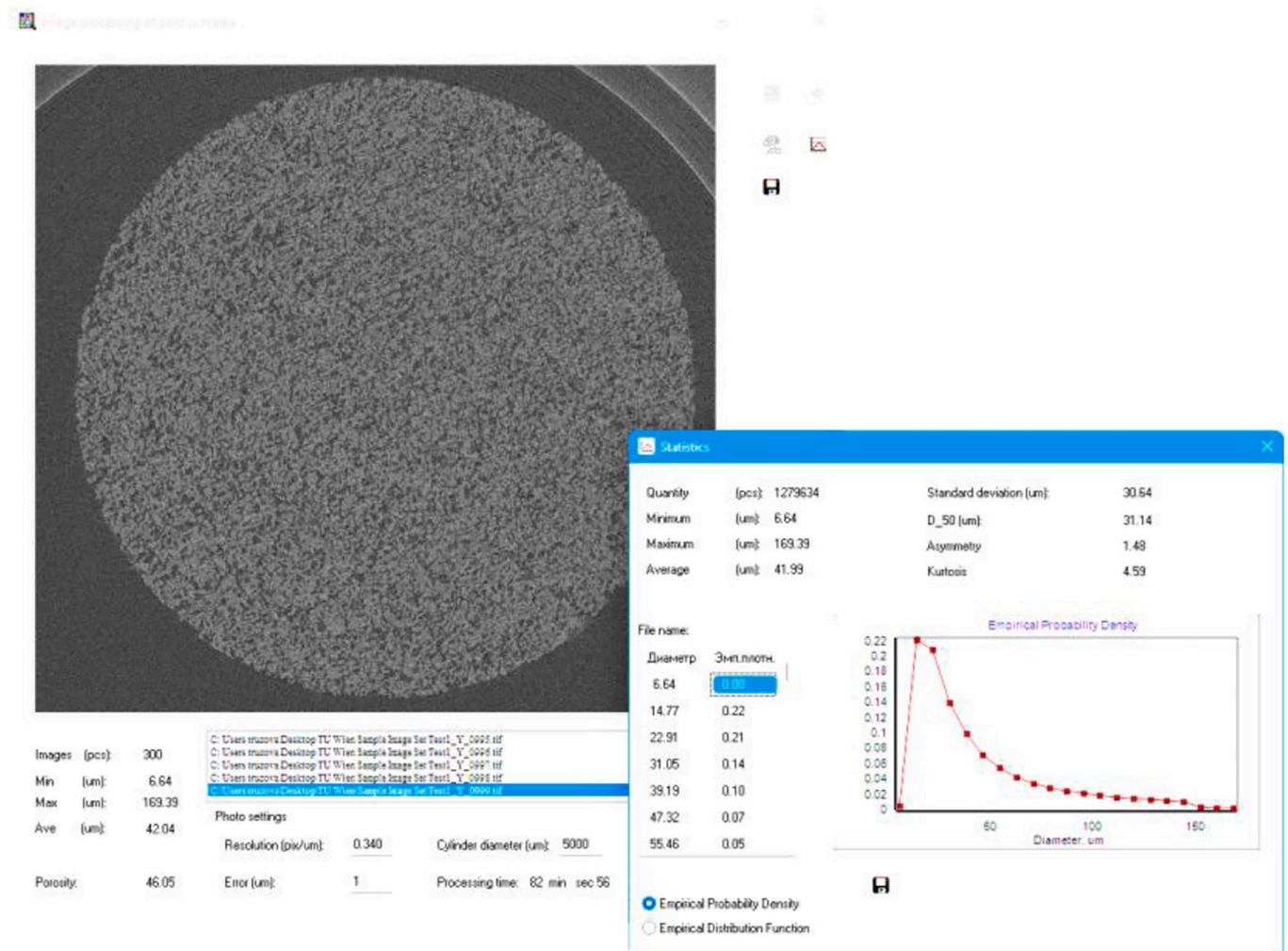

Fig. 17. Software environment.

n–sample size;

x_{min} and x_{max} – the lowest and the highest values in the data set, respectively.

In the lack of information about distribution type, all these five estimates of the center should be calculated and one of them (X_{ctr}) that has a median position should be taken. Authors suggest that such statistic is unaffected by outliers. Using this value, sample censoring bounds are calculated and the values that are beyond the obtained interval are removed:

$$x_{gr} = x_{ctr} \pm t_{gr}s, \tag{3}$$

where

$$t_{gr} = 1.55 + 0.8\sqrt{Kurt - 1} \; lg(n/10),$$

s - standard deviation;

Kurt – kurtosis.

2.10. Software

The proposed strategy was implemented as a software developed in the Embarcadero® Delphi 11 Rapid Application Development (RAD) environment. The developed software fully automated the process of image processing, objects identification and mathematical analysis of obtained data. It formalizes the investigation of the porous media microstructure by means of their images and consists of several interconnected blocks, implementing a certain stage of the processing chain: bitmap unpacking, FOV clipping, image segmentation, artifact removal, pores separation and identification, local separation of large objects, measuring and statistical analysis and outliers removing. A screenshot of the developed software environment is provided in Fig. 17.

Software is provided for illustrative purposes, only to demonstrate the capabilities of the methodology described. Otherwise, parameters such as frame size, FOV size, brightness range etc. as well as switching between fixed/adaptive thresholding may be added to the software interface. The choice of other parameters may be determined by the specificity of the problem in each particular case.

Runtime of our algorithm is approximately 18 s per slice (3500–4000 objects/slice). Runtime optimization is achieved by several factors. One of them is FOV clipping, since the FOV size is usually much smaller than the frame size. Besides, since the contours have been detected, the algorithm deals with the list of contour points, rather than entire bit matrix, that leads to significant calculations speedup.

3. Results and discussion

3.1. Calculation results for different thresholds

The obtained porosity distribution parameters and diagrams for different variants of calculation are shown below in Table 1 and Fig. 18.

Regardless of the pre-specified pore size separation threshold, positively-skewed and sharp-peaked distributions are obtained (Fig. 18). As can be seen from Table 1, as the threshold decreases, the skewness and kurtosis values show a downward trend. The variability of the

Table 1
Porosity distribution parameters.

Parameter/pore size threshold	200 µm	150 µm	120 µm
Porosity, %	48.91	46.05	42.67
Minimum diameter, µm	6.64	6.64	6.64
Maximum diameter, µm	**199.98**	*169.39*	*169.39*
Average diameter, µm	43.49	42.04	40.02
SD, µm	35.39	30.64	26.47
D_{50}, µm	30.24	31.14	31.19
Skewness	1.91	1.48	1.20
Kurtosis	6.60	4.59	3.62

skewness in the considered range of thresholds (200–120 µm) is about 46%, and the kurtosis variability – is about 60%. The variability of each of the mentioned parameters is calculated as the difference between their values obtained at different thresholds, divided by the average value of this parameter. For example, the kurtosis variability ΔKurt in the threshold range Th$_i$ – Th$_j$ was calculated as follows:

$$\Delta Kurt_{Th_i - Th_j} = \frac{\left| Kurt_{Th_i} - Kurt_{Th_j} \right|}{\sum_{k=1}^{M} Kurt_{Th_k} \bigg/ M}, \tag{4}$$

were $Kurt_{Th_i}$, $Kurt_{Th_j}$, $Kurt_{Th_k}$ – kurtosis values corresponding to Th$_i$, Th$_j$, Th$_k$ thresholds ($1 \leq i, j, k \leq M$); M – total measurements number.

Skewness variability was calculated in a similar way. The observed reduction of right skewness (Fig. 18a) may be caused by the decrease in the fraction of large objects due to successful aggregates separation, while the reduction of peakedness can be interpreted as an increase in the "weight" of objects which size corresponds to the area near to the distribution mode. This fact means, that pore diameter size distribution gets more uniform, and may better describe the pore matrix structure.

The nature of the cumulative empirical distribution function also has not changed. In the range of 0–0.8, the curves corresponding to different threshold values almost coincide. This indicates that d_{50} value (diameter below which 50% of the pores are) is practically unaffected by the threshold variation. The variability of d_{50} in the range of 150–120 µm, calculated by a formula similar to (4), is less than 1%, while in the 200–120 µm range – 3%. The relative deviation of d_{50} from the mean value in the entire range is about 1%, except the first variant (200 µm threshold), where deviation is a little higher.

Besides, as the pore separation threshold decreases (Table 1), a noticeable decrease in porosity is observed. The reason for the porosity decrease is that when the pores are separated, the "bridges" connecting them are destroyed, and the percentage of black decreases. Thus, the more separations are performed, the lower porosity value is obtained.

3.2. Edge defects processing

As can be seen in Table 1, despite the fact that in the last two variants separation of all pores over 150/120 µm is performed, the maximum pore size is still about 169 µm (Table 1). Processing the object of maximum size is illustrated below in Fig. 19.

Investigation revealed that mentioned object is a pore located on the side surface of the specimen (Fig. 19 a, b, square green frame). It causes a gap in the section boundary. So, it is impossible to determine exactly whether there is one pore or an aggregate of several pores which septums were broken during the sample molding or cutting (Fig. 19 c, d). Such surface pores are present in a number of images.

A common solution of edge defects problem is a slight reduction of the FOV size by trimming its margins. However, since the investigated specimen is of homogeneous structure, this approach does not completely solve the problem, because, as shown in Fig. 20, when trying to trim margins of any width (Fig. 20b) in the source image (Fig. 20a), other pores are cropped and the same problem occurs at other places (Fig. 20c).

However, to verify this assumption, 60-pixels margins are trimmed (Δ = 60 pixels, ~176 µm), reducing FOV diameter by 7% (Fig. 21). Such significant trimming width should fully demonstrate the efficiency of the mentioned strategy. Corresponding calculations with a pore separation threshold of 150 µm were performed (Table 2).

As expected, data presented in Table 2 suggest that FOV shrinking does not significantly affect distribution parameters (variability of the maximum value is 1.5%, of the kurtosis – 1.7%, and for the average, the skewness and d_{50} values variability is less than 1%).

Due to the reasons described above, boundary pores, as a rule, are statistical outliers. So, they can be removed from the final pore size distribution by means of provided outlier removal technique in section 2.10.
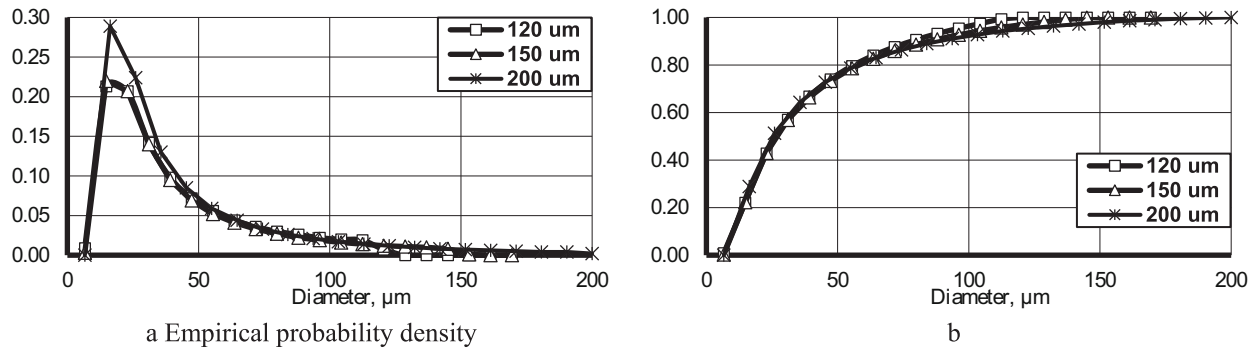
Fig. 18. Pore size distribution curves. Threshold: 200, 150, 120 μm (pores over 200, 150, 120 μm are separated) (a – empirical probability density; b–empirical distribution function)
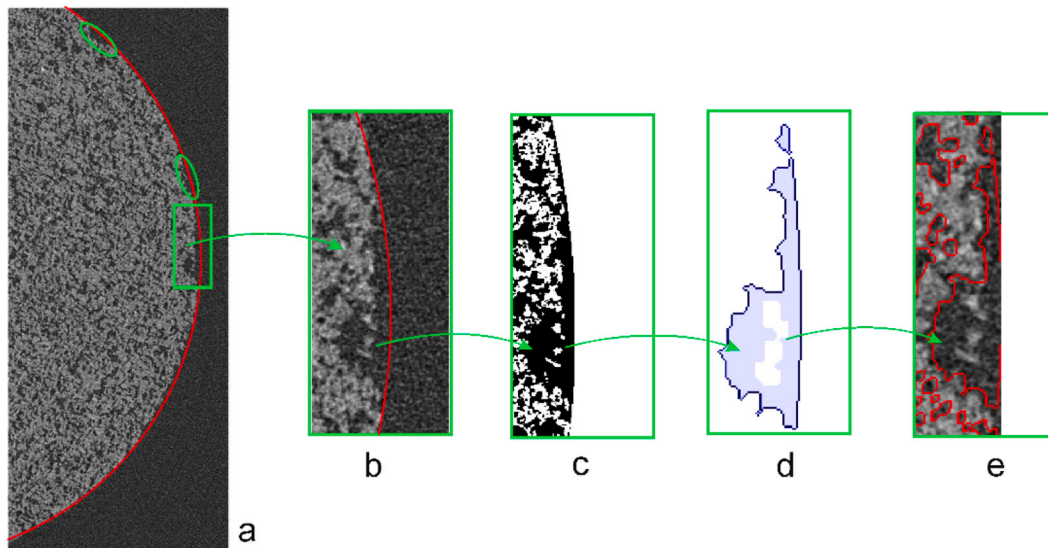

Fig. 19. Pore on the side surface of the specimen a) source image; b) object of interest at high magnification; c) segmented fragment; d) identified object; e) resulting image. Objects of interest are marked in green (square frame – the considered object, oval frame - other similar objects). (For interpretation of the references to color in this figure legend, the reader is referred to the web version of this article.)
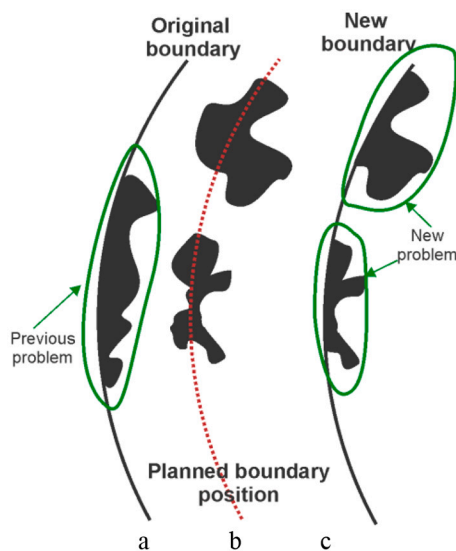

Fig. 20. Arbitrarily placed boundary a) original FOV boundary; b) planned FOV boundary; c) new FOV boundary (green indicates objects that cause a similar problem when shifting the FOV boundary). (For interpretation of the references to color in this figure legend, the reader is referred to the web version of this article.)

3.3. Comparing the results obtained with and without outliers removal

Table 3 and Fig. 22 present results, obtained after outliers removal for 3 variants of the pores separation (with a threshold of 200 μm, 150 and 120 μm).

Figure 21 confirms that in general the nature of the probability density function has not changed. Outliers removal leads to some reduction of asymmetry and peakedness of the probability density function, as confirmed by a decrease of skewness and kurtosis values (Tables 1 and 3). These changes are most pronounced for the 200-μm threshold curve; while for the other two curves the changes were less noticeable (kurtosis variability is 45, 24 and 19%, respectively).

A similar trend was observed in Fig. 18: as the threshold value decreased, the changes between the distribution curves became less significant. This fact may suggest the use of the 200-μm threshold for separating overlapping objects is not efficient enough.

Outliers removal leads to a change in d_{50} value in 1st case (200 μm threshold) – by 4.4%, in 2nd and 3rd cases (150 and 120 μm threshold) – about 7.2 and 7.8%, respectively (Tables 1 and 3). Such significant changes in d_{50} after outliers removal in the last two cases indicate the presence of individual unseparated aggregates, that were interpreted as outliers and removed. This fact generally supports the previous conclusion that assigning thresholds at the level of 120–150 μm in combination with outliers removal may be more appropriate. The applicability of the outlier removal procedure should be assessed
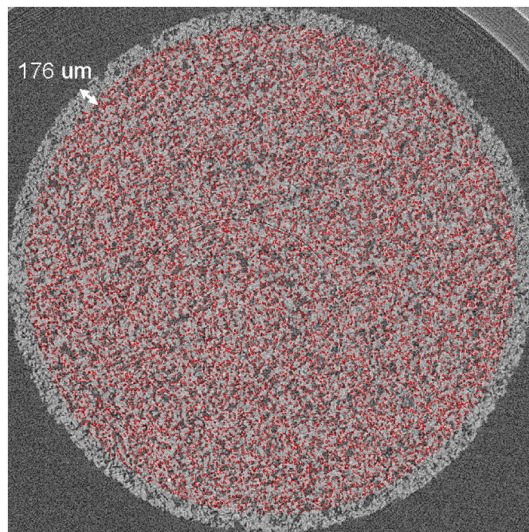
Fig. 21. FOV size shrinking.

Table 2
Porosity distribution parameters with/without edge cutting (pores over 150 μm are separated).

Parameter	Without edge cutting	With edge cutting
Minimum diameter, μm	6.64	6.64
Maximum diameter, μm	*169.39*	*166.96*
Average diameter, μm	42.04	41.81
SD, μm	30.64	30.44
D_{50}, μm	31.14	31.04
Skewness	1.48	1.49
Kurtosis	4.59	4.67

Table 3
Porosity distribution parameters after outliers removal for different pores separation thresholds.

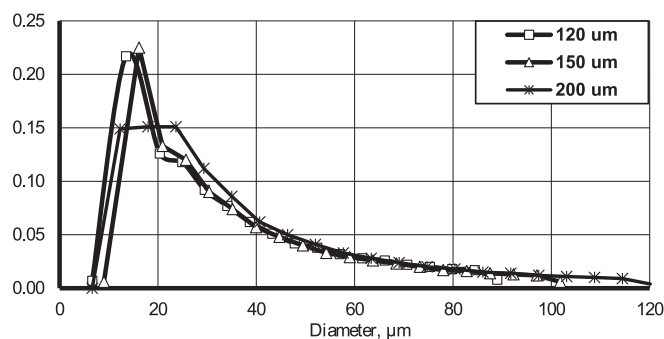| Parameter/pore size threshold	200 μm	150 μm	120 μm
Min, μm	6.64	6.64	6.64
Max, μm	**120.12**	**102.72**	**88.99**
Ave, μm	37.04	36.40	34.31
SD, μm	24.74	21.57	19.79
D_{50}, μm	28.93	28.96	28.85
Skewness	1.34	1.19	0.93
Kurtosis	4.18	3.60	2.98

Fig. 22. Empirical probability density after outliers removal.

considering physical background of the processes that caused formation of large objects (aggregates).

To check the correctness of the proposed technique, it should be compared to the parameters measured by some alternative methods (i. e., not image processing based); in this case the obtained results were in a good agreement with the sample specifications (40–50% for porosity and 30 μm for d_{50}, Table 1). This fact and relative stability of d_{50} even after outliers removal suggests high reliability of the developed technique. However, when analyzing other samples with other set of initial data, proposed technique, can be improved.

4. Conclusions

The paper proposes a robust and effective technique for studying the microstructure of complex and composite materials by their CT images. The developed strategy includes the following steps: bitmap unpacking, FOV selection and clipping, image segmentation, artifacts removal, microobject (pore) separation and denoising, pores identification, local separation of the large (agglomerated) objects, outliers removal (optional), obtaining the resulting image, measuring and statistical analysis. The obtained results were compared with declared porosity and d_{50} values. Obtained data correspond to pre-specified values.

The proposed methodology was used to guide the development of a software that automates the process of microstructure analysis. The advantages of the proposed technique are illustrated on a porous ceramics specimen. Since we used the technique, which is the least dependent on the distribution type for outliers removal, reliability of the developed technique is confirmed and the obtained pore size distribution parameters are meaningful and representative.

A limitation of our study is the fact that the proposed technique is illustrated by means of one type of specimen. Approbation of our methodology on other materials would be of considerable interest.

The paper proposes a simple and effective tool for morphological characterization of the cellular and porous materials. The developed technique can be adapted to study other microenvironments used in various fields of human activity.

Declaration of Competing Interest

The authors declare that they have no known competing financial interests or personal relationships that could have appeared to influence the work reported in this paper.

Data availability

No data was used for the research described in the article.

Acknowledgment

References

[1] S. Ji, Q. Gu, B. Xia, Porosity dependence of mechanical properties of solid materials, J. Mater. Sci. 41 (2006) 1757–1768.

[2] N.H. Thang, Novel porous refractory synthesized from diatomaceous earth and rice husk ash, J. Polym. Compos 8 (2020) 128–137.

[3] S. Simovic, D. Losic, K. Vasilev, Controlled drug release from porous materials by plasma polymer deposition, Chem. Commun. 46 (8) (2010) 1317–1319.

[4] G. Hannink, J.J.C. Arts, Bioresorbability, porosity and mechanical strength of bone substitutes: what is optimal for bone regeneration? Injury 42 (2011) S22–S25.

[5] Y. Li, X. Li, B. Zhu, P. Chen, The relationship between the pore size distribution and the thermo-mechanical properties of high alumina refractory castables, Int. J. Mater. Res. 107 (3) (2016) 263–268.

[6] R. Liu, et al., Influence of pore structure characteristics on the mechanical and durability behavior of pervious concrete material based on image analysis, Int. J. Concr. Struct. Mater. 14 (2020) 1–16.

[7] P. Forquin, A. Arias, R. Zaera, Role of porosity in controlling the mechanical and impact behaviours of cement-based materials, Int. J. Impact. Eng. 35 (3) (2008) 133–146.

[8] L. Jiang, Y. Guan, Pore structure and its effect on strength of high-volume fly ash paste, Cem. Concr. Res. 29 (4) (1999) 631–633.

[9] D. Martinez-Marquez, Y. Delmar, S. Sun, R.A. Stewart, Exploring macroporosity of additively manufactured titanium metamaterials for bone regeneration with quality by design: a systematic literature review, Materials 13 (21) (2020) 4794.

[10] E. Kalatur, S. Buyakova, S. Kulkov, I. Gotman, I. Kocserha, Porosity and mechanical properties of zirconium ceramics, Epitoanyag - J. Silicate Based Compos. Mater. 66 (2014) 31–34, https://doi.org/10.14382/epitoanyag-jsbcm.2014.6.

[11] S. Shimizu, N. Matubayasi, Cooperative sorption on porous materials, Langmuir 37 (34) (2021) 10279–10290.

[12] H. Tanaka, K. Kaneko, A. Matsumoto, K.K. Unger, Rotational state change of acetonitrile vapor on MCM-41 upon capillary condensation with the aid of time-correlation function analysis of IR spectroscopy, in: Studies in Surface Science and Catalysis, Elsevier, 2000, pp. 251–258.

[13] Micromeritics Instrument Corporation, Micromeritics. ASAP 2460. Accelerated Surface Area and Porosimetry System. https://www.micromeritics.com/Repository/Files/ASAP_2460_Brochure.pdf (accessed Mar. 02, 2023).

[14] W. Chen, et al., Simulation study on the effect of pore structure and surface curvature of activated carbon on the adsorption and separation performance of CO_2/N_2, J. Nanopart. Res. 24 (9) (2022) 185.

[15] United States Pharmacopeial Convention, Usp 36-Nf 31 ;United States Pharmacopeia: National Formulary, 36th ed., United States Pharmacopeial Convention, Rockville Md, 2013.

[16] Micromeritics Instrument Corporation, Micromeritics. Application Note. Equilibrated versus Scanning Porosimetry. https://www.micromeritics.com/Repository/Files/ap96.pdf (accessed Mar. 02, 2023).

[17] I.H. Ali, S.H. Kareem, Comparison of mercury intrusion and nitrogen adsorption measurements for the characterization of certain natural raw materials deposits, Baghdad Sci. J. 7 (2010) (1 عدد خاص بمؤتمر العلمي اليوسن‪).

[18] A. Khokhlov, R. Valiullin, M. Stepovich, J. Kärger, Characterization of pore size distribution in porous silicon by NMR cryoporosimetry and adsorption methods, Colloid J. 70 (4) (2008).

[19] J. Mitchell, J.B.W. Webber, J.H. Strange, Nuclear magnetic resonance cryoporometry, Phys. Rep. 461 (1) (2008) 1–36.

[20] T. Svensson, E. Alerstam, J. Johansson, S. Andersson-Engels, Optical porosimetry and investigations of the porosity experienced by light interacting with porous media, Opt. Lett. 35 (11) (2010) 1740–1742.

[21] Q. Libois, F. Lévesque-Desrosiers, S. Lambert-Girard, S. Thibault, F. Domine, Optical porosimetry of weakly absorbing porous materials, Opt. Express 27 (16) (2019) 22983–22993.

[22] A.V. Malinka, Light scattering in porous materials: geometrical optics and stereological approach, J. Quant. Spectrosc. Radiat. Transf. 141 (2014) 14–23.

[23] M. Labus, Comparison of computer image analysis with mercury porosimetry in sandstone porosity measurement, Geol. Quarter. 45 (1) (2001) 75–80.

[24] C.L. Reedy, C.L. Reedy, High-resolution micro-CT with 3D image analysis for porosity characterization of historic bricks, Herit Sci. 10 (1) (2022) 83.

[25] E. Gregorová, W. Pabst, Porosity and pore size control in starch consolidation casting of oxide ceramics—achievements and problems, J. Eur. Ceram. Soc. 27 (2–3) (2007) 669–672.

[26] D. Depriester, R. Kubler, Grain size estimation in polycrystals: solving the corpuscle problem using maximum likelihood estimation, J. Struct. Geol. 151 (2021), 104418.

[27] T. Hildebrand, P. Rüegsegger, A new method for the model-independent assessment of thickness in three-dimensional images, J. Microsc. 185 (1) (1997) 67–75.

[28] R. Ziel, A. Haus, A. Tulke, Quantification of the pore size distribution (porosity profiles) in microfiltration membranes by SEM, TEM and computer image analysis, J. Membr. Sci. 323 (2) (2008) 241–246.

[29] V.A.J. Jaques, et al., Review of porosity uncertainty estimation methods in computed tomography dataset, Meas. Sci. Technol. 32 (12) (2021) 122001.

[30] J.M. Korath, A. Abbas, J.A. Romagnoli, Separating touching and overlapping objects in particle images-a combined approach, Chem. Eng. Trans. 11 (2007) 167–172.

[31] A. El Mallahi, F. Dubois, Separation of overlapped particles in digital holographic microscopy, Opt. Express 21 (5) (2013) 6466–6479.

[32] T. Zou, T. Pan, M. Taylor, H. Stern, Recognition of overlapping elliptical objects in a binary image, Pattern. Anal. Applic. 24 (3) (2021) 1193–1206.

[33] A.I. Rahaghi, U. Lemmin, D. Sage, D.A. Barry, Achieving high-resolution thermal imagery in low-contrast lake surface waters by aerial remote sensing and image registration, Remote Sens. Environ. 221 (2019) 773–783.

[34] B. Schaffer, W. Grogger, G. Kothleitner, Automated spatial drift correction for EFTEM image series, Ultramicroscopy 102 (1) (2004) 27–36.

[35] T. Pavlidis, Algorithms for Graphics and Image Processing, Springer Science & Business Media, 2012.

[36] T.O. Ruzova, Model of threshold classification for the images of dispersed formations, in: Scientific Bulletin of National Mining University.–Dniepropetrovsk (in Russian) Vol. 29, 2007, pp. 162–167.

[37] F.E. Boas, D. Fleischmann, et al., CT artifacts: causes and reduction techniques, Imaging Med. 4 (2) (2012) 229–240.

[38] J.F. Barrett, N. Keat, Artifacts in CT: recognition and avoidance, Radiographics 24 (6) (2004) 1679–1691.

[39] A.M. Raid, W.M. Khedr, M.A. El-Dosuky, M. Aoud, Image restoration based on morphological operations, Intern. J. Comput. Sci. Eng. Inform. Technol. (IJCSEIT) 4 (3) (2014) 9–21.

[40] T.A. Ruzova, V.I. Yeliseyev, A.P. Tolstopyat, L.A. Fleer, Color-subspace model for identification the objects in the images of dispersed systems, in: III international scientific and technical conference "Mathematical and Software Support for intelligent systems". Dnepropetrovsk (in Russian), 2005, p. 154.

[41] T.A. Ruzova, Measurement of geometrical parameters of dispersed structures and three-dimensional objects by their images, in: Optical flow investigation methods: Proceedings of the IX International Scientific and Technical Conference, June 26–29, 2007, Moscow: Publishing house of Moscow Power Engineering Institute (in Russian), 2007, pp. 22–25.

[42] B.V. Anisimov, V.D. Kurganov, V.K. Zlobin, Image Recognition and Digital Processing, Vysshchaia Shkola (in Russian), Moscow, 1983.

[43] T.A. Tolstopyat, O.N. Karpov, V.I. Eliseyev, Evaluation of the particles geometric characteristics using the analytical representation of the contour, in: Issues of Applied Mathematics and Mathematical Modeling. Scientific Bulletin. Dnepropetrovsk: RVV DNU (in Russian) 1, 2001, pp. 104–109.

[44] T.A. Ruzova, O.N. Karpov, L.A. Fleer, Routine Monitoring of Individual Parameters of Dispersive Structures 2, Scientific Bulletin of the National Mining University, Dnipropetrovsk. (in Russian), 2004, pp. 83–88.

[45] P.V. Novitsky, I.A. Zograf, Evaluation of Measurement Result Errors, Energoatomizdat (in Russian), Leningrad, 1985.

[46] Y.A. Rudzit, V.N. Plutalov, Fundamentals of Metrology, Accuracy and Reliability in Instrumentation, Mechanical Engineering (in Russian), Moscow, 1991.